ADVANCES IN ATMOSPHERIC SCIENCES, 2026

• **Data Paper** •

Dataset of China Kuroshio Extension Observatory (CKEO): Moored Buoy Observations in the Kuroshio–Oyashio Transition Zone

Zhaohui CHEN[1], Yueqi ZHANG[1], Ruichen ZHU[2], Zhongxiang FAN[1], Jia-Zhen WANG[2], Xin MA[*1], Guoqing REN[1], Haiyuan YANG[1], Lixiao XU[1], Xiaopei LIN[1], and Lixin WU[1,2]

[1]*Ocean University of China*, *Qingdao* 266100, *China*

[2]*Laoshan Laboratory*, *Qingdao* 266237, *China*

(Received 29 September 2025; revised 16 December 2025; accepted 23 December 2025)

ABSTRACT

The Kuroshio–Oyashio Transition Zone (KOTZ) serves as a vital dynamic interface between the warm Kuroshio Extension and the cold Oyashio Current. However, severe sea conditions with strong ocean currents, winds and waves pose challenges for sustained in situ observations of both oceanic and atmospheric variables. This paper introduces the China Kuroshio Extension Observatory (CKEO), a moored observatory program designed for long-term observations in the KOTZ. We provide a dataset of meteorological and oceanographic properties, including sea surface wind, air temperature, atmospheric pressure, relative humidity, sea surface temperature, sea surface salinity, ocean currents in the upper 100 m, and temperature profile in the upper 500 m. The CKEO, which began operations in 2019, provides a continuous air–sea observational dataset of the KOTZ to the scientific community and advances the understanding of multiscale physical processes in this region.

Key words: Kuroshio–Oyashio Transition Zone, China Kuroshio Extension Observatory, moored buoy, observational dataset

Citation: Chen, Z. H., and Coauthors, 2026: Dataset of China Kuroshio Extension Observatory (CKEO): Moored buoy observations in the Kuroshio-Oyashio transition zone. *Adv. Atmos. Sci.*, https://doi.org/10.1007/s00376-025-5673-1.

Dataset profile

Dataset title	Dataset of China Kuroshio Extension Observatory (CKEO): Moored Buoy Observations in the Kuroshio–Oyashio Transition Zone
Time range	September 2019–September 2025
Geographical scope	39°N, 149.2°E (September 2019–June 2021); 39°N, 149.6°E (June 2021–September 2025)
Data format	nc
Data volume	24.4 MB
Data service system	https://doi.org/10.57760/sciencedb.j00264.00002 https://doi.org/10.5281/zenodo.16569633
Dataset composition	The dataset consists of four files: CKEO_ATM_QC.nc containing meteorological data after QC procedures; CKEO_ATM_RAW.nc containing raw meteorological data with quality flags; CKEO_ADCP.nc containing current measurements; and CKEO_Tprofile.nc containing ocean temperature profiles.

1. Introduction

The Kuroshio–Oyashio Transition Zone (KOTZ) lies between the warm Kuroshio Extension (KE) and the cold Oyashio Extension, marking the subtropical–subpolar gyre boundary in the Northwest Pacific (Fig. 1). It is a key formation region for large-scale mode waters that ventilate and redistribute heat, freshwater, and nutrients across the North Pacific (Jutras et al., 2025; Liu et al., 2025). The KOTZ is also replete with complex frontal structures (Iwao et al., 2003; Yasuda, 2003), energetic meso- and submesoscale eddies (Qiu and Chen, 2005; Itoh and Yasuda, 2010; Chelton et al., 2011; Sasaki and Minobe, 2015; Su et al., 2018; Yang et al., 2018), thereby exerting profound impacts on climate, ecosystems, and fisheries (Polovina et al., 2006; Kwon et al., 2010; Frankignoul et al., 2011; Yatsu et al., 2013; Yamamoto et al., 2018; Di Lorenzo et al., 2023; Li et al., 2025).

The confluence of the Kuroshio and Oyashio produces sharp sea surface temperature (SST) gradients, which enhance atmospheric baroclinicity and favor frequent storm

* Corresponding author: Xin MA
Email: maxin@ouc.edu.cn

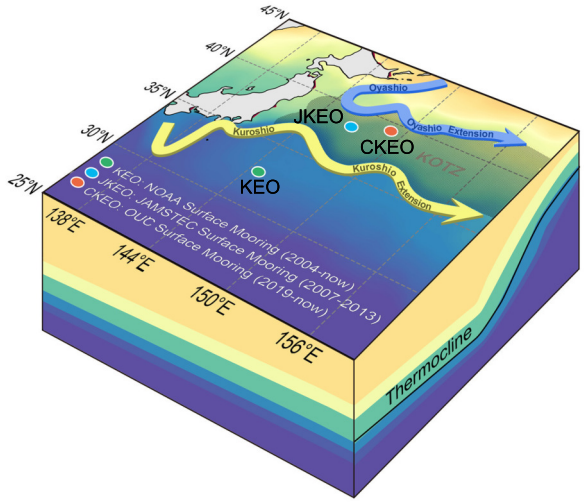

Fig. 1. Map of the Northwest Pacific with surface moorings (green, KEO/NOAA; blue, JKEO/JAMSTEC; red, CKEO/OUC). Gray hatching: KOTZ.

development. In turn, the passing storms (Alford, 2003; Liu et al., 2019) and typhoons (Bond et al., 2011; Tsopouridis et al., 2021) inject substantial near-inertial kinetic energy into the upper ocean. The resultant intense near-inertial motions, together with nonlinear eddy interactions, drive energy cascades and greatly enhance turbulent mixing, efficiently regulating the thermal structure of the upper ocean (Jing and Wu, 2014; Nagai et al., 2015; Whalen et al., 2020).

Mesoscale air–sea interactions in the KOTZ are vigorous, with oceanic mesoscale eddy–atmosphere coupling modulating precipitation, storms, and circulation (Small et al., 2008; Frenger et al., 2013; Ma et al., 2017; Czaja et al., 2019; Foussard et al., 2019; Gan et al., 2023; Seo et al., 2023). The critical importance of such regional air–sea dynamics is globally recognized, underscoring the necessity for comprehensive observations, as highlighted by initiatives like the UN Decade Observing Air–Sea Interactions Strategy (OASIS; Cronin et al., 2023a). A central mechanism is the thermal coupling between SST and turbulent heat fluxes (Ma et al., 2024), which acts both as an atmospheric energy source fueling weather systems (e.g., Renault et al., 2019; Liu et al., 2021) and an oceanic energy sink dissipating eddy energy (Ma et al., 2016; Jing et al., 2020).

However, from an observational perspective, the KOTZ still lacks systematic long-term measurements. While fixed-point arrays such as TAO/TRITON, Research Moored Array for African-Asian-Australian Monsoon Analysis and Prediction (RAMA), and PIRATA provide valuable records in tropical oceans (McPhaden et al., 2023), mid- to high-latitude oceans remain a "desert" for sustained ocean–atmosphere observations because of strong currents, high winds, and harsh sea states. To address this issue, the National Oceanic and Atmospheric Administration (NOAA) established the Kuroshio Extension Observatory (KEO) in June 2004, south of the KE (~32.3°N, 144.6°E). The KEO, an upgraded Tropical Atmosphere Ocean (TAO) mooring designed to withstand extreme KE conditions, carries both meteorological and oceanographic sensors and has provided valuable continuous estimates of air–sea fluxes in this energetic region (Cronin et al., 2008, 2023b).

Between 2007 and 2013, the Japan Agency for Marine-Earth Science and Technology (JAMSTEC) initiated the JAMSTEC Kuroshio Extension Observatory (JKEO), further north at (38.0°N, 146.4°E) (Tomita et al., 2021). However, after 2014, no subsequent long-term surface mooring was maintained to the north of the KE, resulting in a loss of simultaneous observations across the KE front. The discontinuation of these high-resolution datasets—capable of resolving eddies, fronts, and storm-track activity—significantly limits understanding of meso- and submesoscale processes and their climate impacts.

The China Kuroshio Extension Observatory (CKEO), a surface moored buoy, has been deployed north of the KE jet since 2019 and maintained by the Ocean University of China. As a key part of China's Kuroshio Extension Mooring Array, it provides direct monitoring of the air–sea interface in the KOTZ, which is crucial for investigating multiscale processes like storm tracks, oceanic eddies, and marine heatwaves. This paper introduces the CKEO, describing its design (section 2), data (section 3), and preliminary observational results (section 4). Two case studies of eddy and typhoon passages are presented in section 5, followed by a summary and discussion in the final section.

2. CKEO buoy

The CKEO features a disc-shaped cylindrical body, comprising an upper buoy tower and a lower section connected to an anchoring system. The tower is generally designed as a truss structure, featuring a bowl-shaped top that houses various equipment, including meteorological sensors, an Iridium communication system, a power supply system, and a safety warning system. The anchoring system consists of a gravity anchor, chains, ropes, and inductive cables (Fig. 2).

2.1. *Mooring system*

Open-ocean buoys generally use taut-line or slack-line moorings. In the KOTZ, strong currents and rough seas impose high static and dynamic loads, making taut-line systems vulnerable to failure. Therefore, the CKEO buoy adopts a slack-line design with an aspect ratio of ~1.5:1 (an 8500 m line at a 5650 m depth) to reduce stress and enhance survivability. The observation section employs inductive coupling, and recovery is enabled by dual EdgeTech 8242XS acoustic releases attached to a set of glass floats. The anchor, weighing 4 tons (train wheels), is left on the seabed after recovery.

The mooring line combines 4500 m of nylon rope (Ø20 mm, >10-ton strength) in the upper segment and 3500 m of polypropylene rope (Ø20 mm, >7-ton strength) in the lower segment. The nylon rope is coated with a rubberized, wear-resistant layer and equipped with 12 floats for extra buoyancy. Standard shackles, swivels, and pear-shaped rings miti-

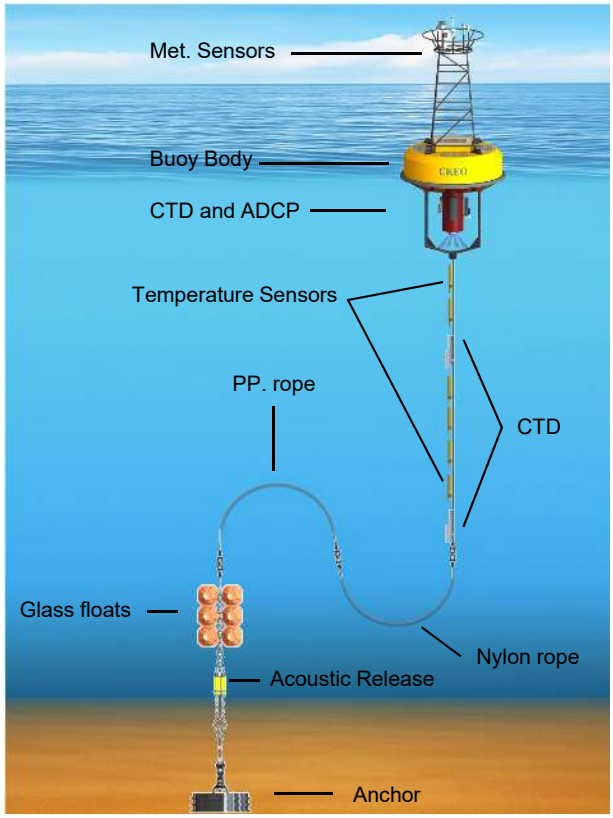

Fig. 2. Overall design of the CKEO.

gate torsion and vibration, enhancing durability and operational safety.

The buoy body is constructed from a magnesium–aluminum alloy, which provides high strength, low density, and strong corrosion resistance, though it is ~20% heavier than foam-filled buoys. A suspension system with double-point load and a low-mounted battery compartment lowers the center of gravity and separates it from the center of buoyancy, minimizing capsizing risk and enabling long-term stability under extreme sea conditions.

2.2. *Sensor suite*

The CKEO carries a suite of sensors to measure wind speed and direction (WS and WD), air temperature (AT), atmospheric pressure (AP), relative humidity (RH), shortwave and longwave radiation (SWR and LWR), SST, sea surface salinity (SSS), upper-ocean currents (0–100 m), and subsurface temperature (to 500 m). Notably, the CKEO only carried meteorological sensors and a conductivity–temperature–depth sensor (CTD) during the initial deployment phase (2019–22). From 2022 onward (CKEO-04 and follow-up buoys), an acoustic Doppler current profiler (ADCP) was added to measure ocean currents in the upper 100 m. Beginning in 2023 (CKEO-05 and follow-up buoys), the system was further upgraded with a set of inductive temperature loggers (T), temperature–depth sensors (TD), and CTDs, enabling real-time measures of temperature, depth, and salinity throughout the upper 500 m.

Meteorological measurements are made primarily with the MaxiMet GMX600 automatic weather station (including WS, WD, AT, AP and RH), with VAISALA PTB210 and HMP155 as backups. SWR and downward LWR are measured using EPLAB SPP and PIR sensors, respectively; from 2024 onward, radiation sensors from Hukseflux replaced the EPLAB instruments. The Seabird SBE-37SM is used as the CTD, which is mounted on the bottom of the buoy body along with a WHS-300K ADCP for current profiling in the upper 100 m. A suite of inductive temperature loggers, TDs, and CTDs are attached to the cable in the upper 500 m for real-time monitoring (Table 1 summarizes the instruments and observed parameters, and Table 2 details the sensor depths for different CKEO deployments).

2.3. *Control/communication system*

The control/communication system of the CKEO integrates data acquisition, control, communication, and power supply functions. Sampling strategies are optimized according to sensor type and scientific objectives. Currently, the data acquisition frequency for meteorological and underwater sensors is 1 h (see Table 1 for details). All raw data are archived, while transmitted data undergo both real-time and delayed quality control (QC). Meteorological observations are processed with real-time 3σ outlier removal and averaging before transmission, whereas instantaneous measurements (e.g., CTD/TD/T) are subject only to delayed QC. Processed datasets are relayed via the Iridium satellite network. The power system consists of sixteen 100 Ah lead-acid batteries and four 60 W solar panels, supporting an average current of ⩽0.4 A (⩽4.8 W) with 2 min of operation every 10 min, corresponding to an annual consumption of ~700 Ah. This configuration enables at least one year of autonomous deployment in open-ocean environments.

3. Data collection and integrity

Since 2019, we have successfully deployed seven CKEO buoys and recovered six of them to date (Fig. 3, Table 3). All CKEO buoys are named sequentially as CKEO-01, CKEO-02, CKEO-03, CKEO-04, CKEO-05, CKEO-06, and CKEO-07. This deployment strategy follows an approximately annual replacement cycle, wherein each buoy system operates for nearly one year before recovery and subsequent deployment of the next buoy. The nominal position of the CKEO is (39°N, 149.2°E), and this position has been shifted eastward by about 24 nautical miles (~33 km) since 2021 to minimize disruptions caused by fishing activity. Due to various factors, such as buoy damage from harsh waves, failures in the control/communication system and potential sabotage by nearby fishermen, the mean operational duration across all deployed CKEO buoys is approximately 209 days per year, calculated from initial deployment to the last successful data transmission.

3.1. *Delayed data QC*

The raw data transmitted via the Iridium satellite communication system undergo comprehensive delayed QC proce-

Table 1. Parameters measured by the CKEO.

Mounting height	Parameter	Model	Sampling frequency	Data retrieval
4 m above sea surface	WS, WD, AT, AP, RH	MaxiMet GMX600	1 Hz	Mean of first 2 min of each hour (CKEO-01/02/03/04)
	AT*, RH*	Vaisala HMP155	1 Hz	
	AP*	Vaisala PTB210	1 Hz	Mean of last 2 min of each hour (CKEO-05/06/07)
	SWR	EPLAB SPP	1 Hz	Mean of first 2 min of each hour (CKEO-01/02/03/04/05)
		Hukseflux SR30	0.5 Hz	Mean of last 2 min of each hour (CKEO-06/07)
	LWR	EPLAB PIR	1 Hz	Mean of first 2 min of each hour (CKEO-01/02/03/04/05)
		Hukseflux IR20	0.5 Hz	Mean of last 2 min of each hour (CKEO-06/07)
1.5 m below sea surface	ocean current speed, current direction	WHS-300K ADCP	1 ping per second	Mean of first minute of each hour
0.4 m below sea surface	SST, SSS	Seabird SBE-37SM	hourly	hourly
5–500 m below sea surface	subsurface T	Enduro AT S9		
	subsurface CTD	Seabird SBE-37IM		
	subsurface TD	Seabird SBE-39IM TD		

*Backup sensor

Table 2. Layout of subsurface measurements by the CKEO.

Nominal depth (m)	CKEO-05	CKEO-06	CKEO-07
5	T	T	T
10	T	T	T
20	T	T	T
30	T	T	T
40	T	T	T
50	T	T	T
60	T	T	T
70	–	–	T
80	T	T	T
90	–	–	T
100	T	TD	CTD
120	T	T	–
150	T	T	–
200	TD	TD	TD
300	T	T	T
500	TD	CTD	CTD

dures to ensure data integrity and reliability for subsequent scientific analysis. The primary stage of QC involves the removal of default values generated during transmission failures or communication interruptions. Subsequently, range checks are applied based on the expected physical boundaries and climatological characteristics of each variable. Values that exceed the predetermined bounds are flagged and removed from the dataset, as they likely result from sensor malfunctions, transmission errors, or extreme outlier events that are incompatible with local environmental conditions. The final QC procedure employs a statistical outlier detection algorithm applied to sequential data segments. For a certain number of consecutive measurements of each variable, values that exceed three standard deviations (3σ) from the segment mean are identified as statistical outliers and subsequently removed.

3.2. *Data integrity*

After delayed QC, the consolidated CKEO dataset is publicly available (https://doi.org/10.57760/sciencedb.j00264.00002; https://doi.org/10.5281/zenodo.16569633). Figure 4 illustrates the data availability following the implementation of delayed QC procedures. The data acquisition rate, defined as the ratio of hourly data records retained after QC to the total expected number of hourly records over each buoy's operational period, reaches only 60% across CKEO-01 to CKEO-07. It is worth noting that data from CKEO-07 are shown as of mid-September 2025, with the buoy currently on-site and functioning normally.

Interannual variability in data acquisition rates is observed across the CKEO deployment timeline. Since the initial aim of deploying the CKEO buoys was to calculate air–sea heat flux, the meteorological sensors and CTD at the sea surface were installed on the buoys from the initial deployment phase (CKEO-01) in 2019. The data acquisition rate for meteorological data is generally high, except during the first half of 2022 and for CKEO-05 and CKEO-06, when data coverage was markedly reduced. Similar gaps are evident in the ADCP (which started operating from CKEO-04) and in the subsurface temperature measurements (available from CKEO-05 onward). The causes of these discontinuities, particularly for CKEO-03, CKEO-05, and CKEO-06, are addressed in the discussion section. Compared to the relatively high acquisition rate of meteorological variables, SST and SSS data exhibit substantially lower completeness, particularly during the initial three years of CKEO deployment. Closer inspection indicates that the CTD mounted at the base of the buoy is especially vulnerable to biofouling by barnacles and other marine organisms, which frequently leads to elevated noise levels, long-term drift, or outright data loss in salinity records.

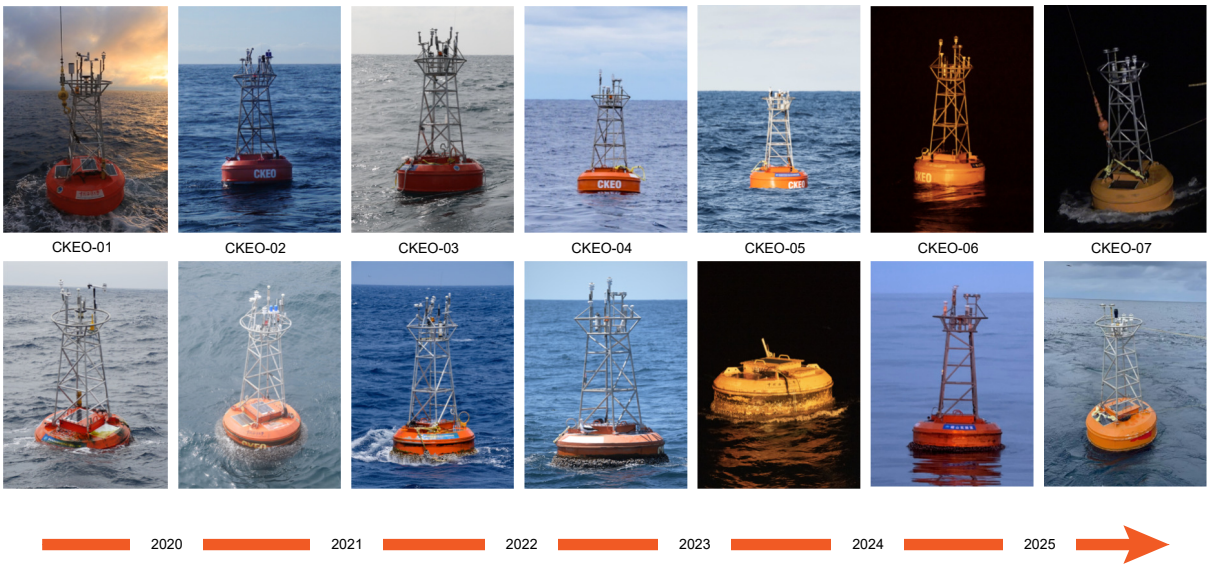

Fig. 3. Photos of the CKEO buoy taken during deployment (upper panels) and recovery (lower panels) from each cruise. Note that CKEO-07 was just deployed in May 2025 and remains currently active on site. For CKEO-05, the upper structure was intentionally destroyed by fishermen.

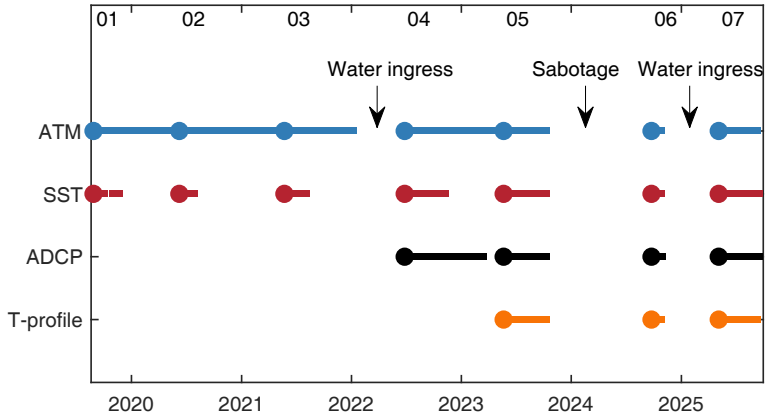

Fig. 4. Statistics of key data acquisition for CKEO buoys. ATM: meteorological data (blue); SST: sea surface temperature data (red); ADCP: ocean current data in the upper 100 m (black); T-profile: subsurface temperature data in the upper 500 m (orange).

Table 3. Deployment and recovery dates and positions of the CKEO.

Buoy ID	Longitude (°E)	Latitude (°N)	Deployment date	Recovery date
CKEO-01	149°16.32'	38°59.59'	2019/09/06	2020/06/16
CKEO-02	149°13.28'	39°01.41'	2020/06/17	2021/06/02
CKEO-03	149°36.72'	38°59.63'	2021/06/02	2022/06/29
CKEO-04	149°38.21'	38°59.31'	2022/07/06	2023/05/25
CKEO-05	149°38.32'	38°59.29'	2023/05/31	2024/10/03
CKEO-06	149°38.38'	38°58.03'	2024/10/03	2025/05/15
CKEO-07	149°38.41'	38°57.08'	2025/05/15	2025/10/24*

*The CKEO-07 buoy went adrift in early October due to fishing activities. It was recovered by RV DFH3 on 24 October 2025.

4. Basic characteristics of CKEO observations

4.1. *Atmospheric and ocean surface variables*

Figure 5 shows that, despite substantial data gaps, the time series of meteorological variables and SST/SSS exhibit a clear annual cycle. The AP observed by the CKEO generally ranges from 1000 hPa to 1030 hPa, with occasional drops below 980 hPa, indicative of strong storms or typhoons traversing the area. RH mostly lies between 60% and 100%, also with an evident annual cycle. WS is generally over

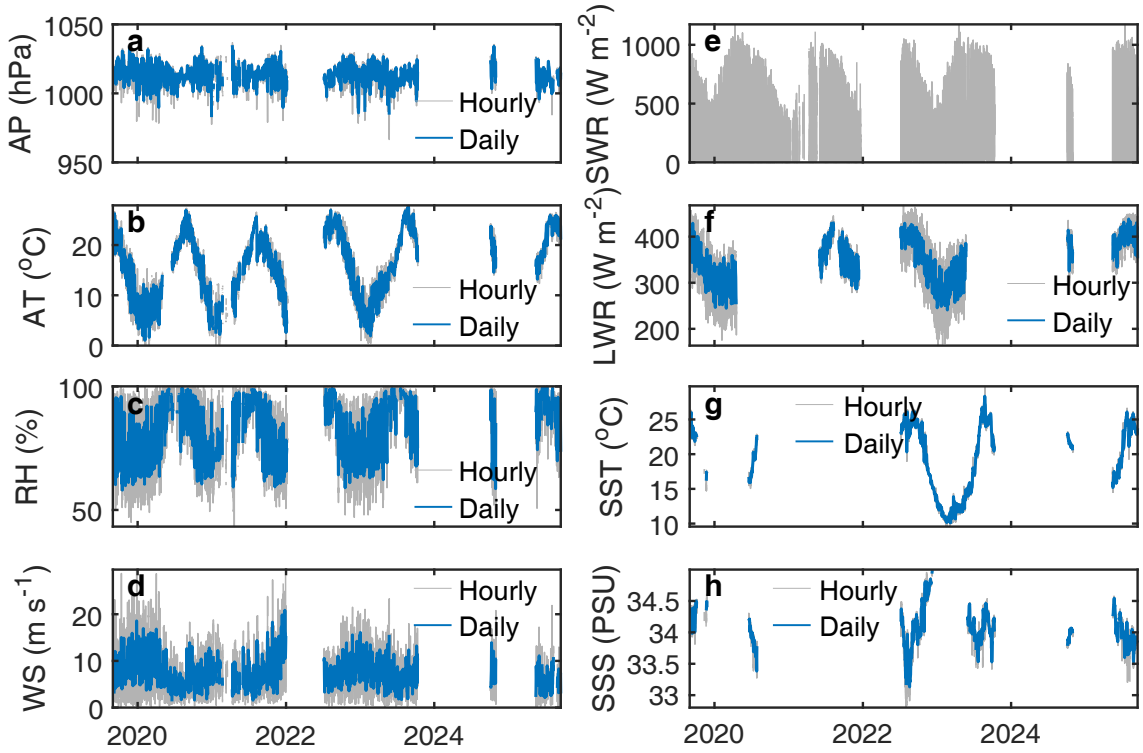

Fig. 5. Time series of hourly (gray) and daily (blue) variables collected by the CKEO buoys: (a) AP, (b) AT, (c) RH, (d) WS, (e) SWR, (f) LWR, (g) SST, (h) SSS.

8 m s^{-1}, and sometimes exceeds 20 m s^{-1}. These high-wind episodes are unevenly distributed among years and tend to co-occur with periods of reduced AP, indicating a linkage between wind intensification and low-pressure passages.

SWR has distinct diurnal and seasonal cycles, with daily maxima exceeding 1000 W m^{-2} in summer, but much lower in winter. The downward LWR generally lies between 250 W m^{-2} and 450 W m^{-2}. The QC process identified instances of sensor failure in the raw LWR data. These issues, potentially related to sensor configuration or build quality, have been flagged accordingly in the raw data.

AT ranges from 0°C to 28°C, while the lowest SST only reaches 10°C, suggesting that the KOTZ region is a hotspot for oceanic heat loss during winter. SSS varies between 33.0 PSU and 35.0 PSU, showing significant intraseasonal variability. Some sharp drops in surface salinity may be related to local heavy precipitation or the intrusion of low-salinity Oyashio water.

4.2. *Subsurface temperature, salinity and ocean currents*

The temperature profile measurements reveal distinct thermal stratification throughout the upper 300 m (Fig. 6a). The temperature exhibits a typical thermocline structure, with surface temperatures ranging from 18°C to 24°C in the upper 50 m and further decreasing to 8°C below 250 m. A notable thermal anomaly occurred in October 2023, characterized by significant subsurface warming that penetrated to ~300 m and persisted for several weeks. This warming event, with temperature anomalies exceeding 4°C–6°C relative to the seasonal mean, coincided temporally with strong velocity signals observed in the ADCP measurements, suggesting the passage of a warm-core anticyclonic eddy through the mooring site. A detailed dynamical analysis of this event is provided in section 5.

The ocean currents in the upper 100 m are largely barotropic, as indicated by their uniform vertical structure, implying dominance of large-scale pressure-gradient forcing (Figs. 6b, c). A comparison between depth-averaged ADCP velocities and satellite altimetry-derived geostrophic currents is shown in Figs. 6d and e. Their remarkable agreement in the major flow variations indicates that surface geostrophic flow can reasonably approximate the upper-ocean circulation in this region. However, ADCP records exhibit stronger high-frequency variability and higher-amplitude fluctuations, particularly during mesoscale eddy passages. Most importantly, during the identified eddy events in July 2022 and August 2023, the ADCP recorded maximum velocities of around 1 m s^{-1}, while the corresponding altimetry-derived geostrophic velocities underestimated the true magnitude by more than 50%.

4.3. *Turbulent heat flux*

Figure 7 presents the longest continuous record from the CKEO (2022–2023) suitable for estimating turbulent air–sea heat fluxes. Sensible heat flux (SHF) and latent heat flux (LHF) were computed with the COARE 3.0 bulk algorithm (Fairall et al., 2003), with the convention that positive fluxes are upward from the ocean to the atmosphere.

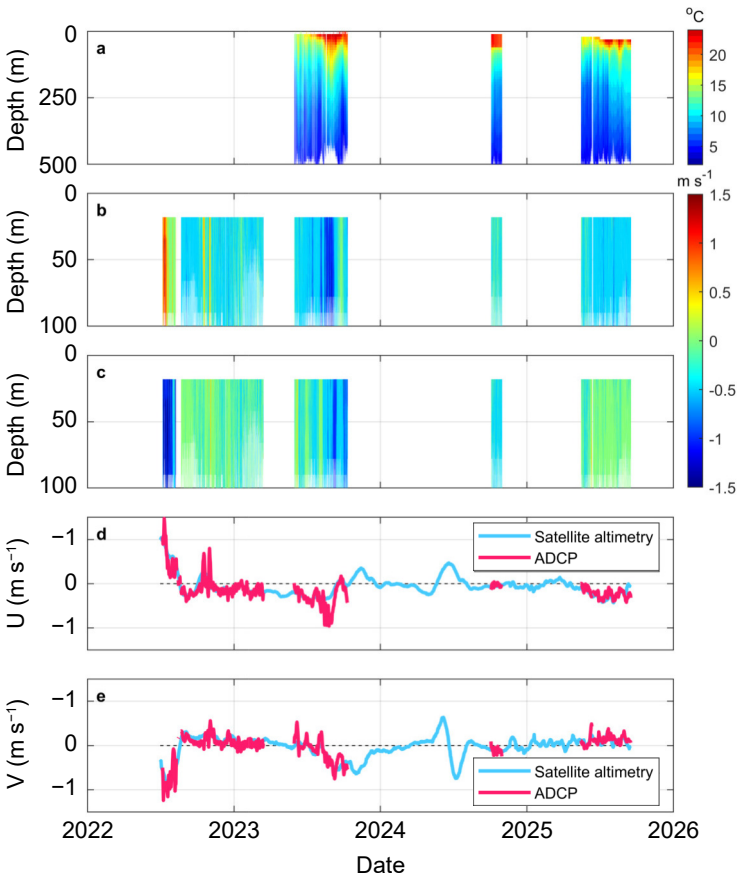

Fig. 6. Depth–time contour plots of (a) temperature and (b) zonal and (c) meridional velocity profiles from the CKEO. Time series comparison of depth-averaged ADCP (d) zonal and (e) meridional velocities with satellite altimetry-derived geostrophic currents sourced from the Copernicus Marine Service's "Global Ocean Gridded L4 Sea Surface Heights And Derived Variables Reprocessed" product (https://dx.doi.org/10.48670/moi-00148).

The seasonal cycle is dominated by strong wintertime ocean heat loss. From late autumn through winter, SHF frequently approaches 200 W m^{-2}, while LHF often exceeds 400 W m^{-2}, producing sustained upward turbulent heat export. In contrast, summer is characterized by weak fluxes and occasional downward events.

SST and AT both display a clear annual cycle peaking in summer. However, their difference (SST minus AT) peaks in winter at about 10°C, when cold, dry continental air overlies relatively warm KE waters. This large positive temperature contrast drives the winter maximum in SHF through enhanced upward sensible heat transfer. During summer, AT often exceeds SST, producing negative SST–AT differences and weak downward SHF (heat transfer from atmosphere to ocean).

The moisture exerts a parallel control on LHF. RH is the lowest in autumn/winter, favoring high evaporation and thus large upward LHF. Conversely, when the marine boundary layer approaches saturation (i.e., RH close to 100%) and AT is relatively high, the COARE algorithm yields negative LHF, indicating downward LHF.

4.4. *Comparison of key variables with ERA5*

To assess the quality of CKEO buoy observations, we compared some key variables with the ERA5 dataset [resolution: hourly, 0.25° (Hersbach et al., 2025)]. ERA5 data are interpolated to the buoy locations and adjusted to sensor heights using the COARE 3.0 algorithm to ensure spatiotemporal coherence (Fairall et al., 2003).

Overall, the agreement is strong (Fig. 8). AT, AP and SST show high correlation ($R > 0.98$) and low errors (RMSE < 1 and MAE < 1. RMSE: root-mean-square error; MAE: mean absolute error), confirming the data reliability. However, WS and RH exhibit more complex features. For WS, while the regression slope is close to unity, the CKEO-measured WS systematically exceeds ERA5 when speeds are >10 m s^{-1}, resulting in an RMSE of ~2 m s^{-1}. For RH, the regression slope of significantly less than 1 indicates a systematic underestimation by ERA5, leading to large errors (RMSE: ~8.37; MAE: ~6.91). These findings are generally consistent with the earlier KEO–ERA5 comparison by Cronin et al. (2008).

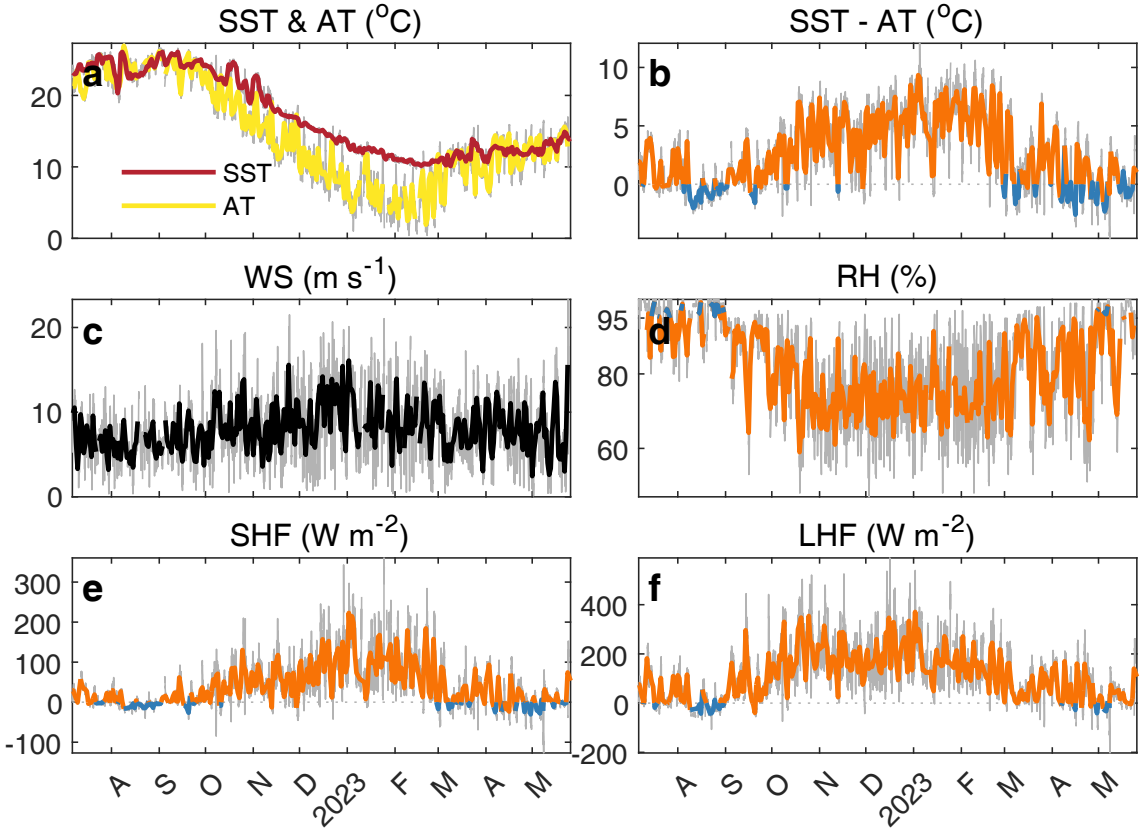

Fig. 7. Air–sea turbulent heat fluxes (upward positive) and related parameters: (a) SST and AT; (b) air–sea temperature (SST minus AT); (c) WS; (d) RH; (e) SHF; and (f) LHF. Gray lines are hourly data, while colored thick lines are daily means. Orange (blue) lines represent the period of upward (downward) heat flux in (b), (d), (e) and (f).

5. Cases where the CKEO captures multi-scale oceanic/atmospheric processes

5.1. *Eddy influence on upper ocean*

From 14 August to 20 September 2023, the moored buoy system recorded a remarkable warming signal extending throughout the upper 300 m and persisting for ~1 month (Fig. 9). This extreme warming event is particularly noteworthy as it occurred concurrently with a well-documented, basin-scale marine heatwave in the Northwest Pacific (e.g., Sugimoto, 2025), and our mooring data appear to have captured a powerful, localized expression of these broader warming conditions. The temperature anomaly exhibited a pronounced vertical structure, with the most dramatic warming occurring at the sea surface where temperatures increased from the pre-event baseline of 17°C to a peak of 24°C. Even at the depth of 200 m, the thermal signal remained robust, with temperature increases of 4°C (Fig. 9d). Concurrently, the ADCP measurements revealed a pronounced intensification of westward currents that maintained similar temporal persistence throughout the warming period (Figs. 9e, f). The current velocity experienced a dramatic acceleration from ~0.2 to ~1.2 m s^{-1}, representing a five-fold increase in magnitude that fundamentally altered the local circulation patterns. The magnitude and persistence of these anomalies cannot be explained by atmospheric forcing alone, pointing to an oceanic origin.

Satellite-derived sea level anomaly (SLA) fields confirm the presence of a warm-core anticyclonic eddy. This eddy can be traced back to 20 July, when the KE underwent a significant meandering event (Fig. 9a). An increasingly pronounced curvature eventually developed into closed SLA contours, leading to the pinch-off and formation of a warm-core eddy with an approximate diameter of ~200 km west of the buoy location (Fig. 9b). After 25 days, the southeastern periphery of the eddy made first contact with the CKEO, generating the observed strong southwestward currents. On 9 September, the eddy started to change its propagation direction from eastward to westward and moved away from the buoy site (Fig. 9c). This departure of the eddy explains the gradual return of temperature and velocity toward background conditions.

5.2. *Responses of atmosphere and ocean to Typhoon Krosa (2025)*

A very recent case is the passage of Typhoon Krosa (2025). From 2 to 3 August 2025, Krosa (2025) passed near the CKEO, moving rapidly at approximately 44 km h^{-1}, exerting a significant impact on the surrounding area. The buoy was generally located on the right-hand side of Krosa (2025)'s track (Fig. 10a), and it successfully captured pro-

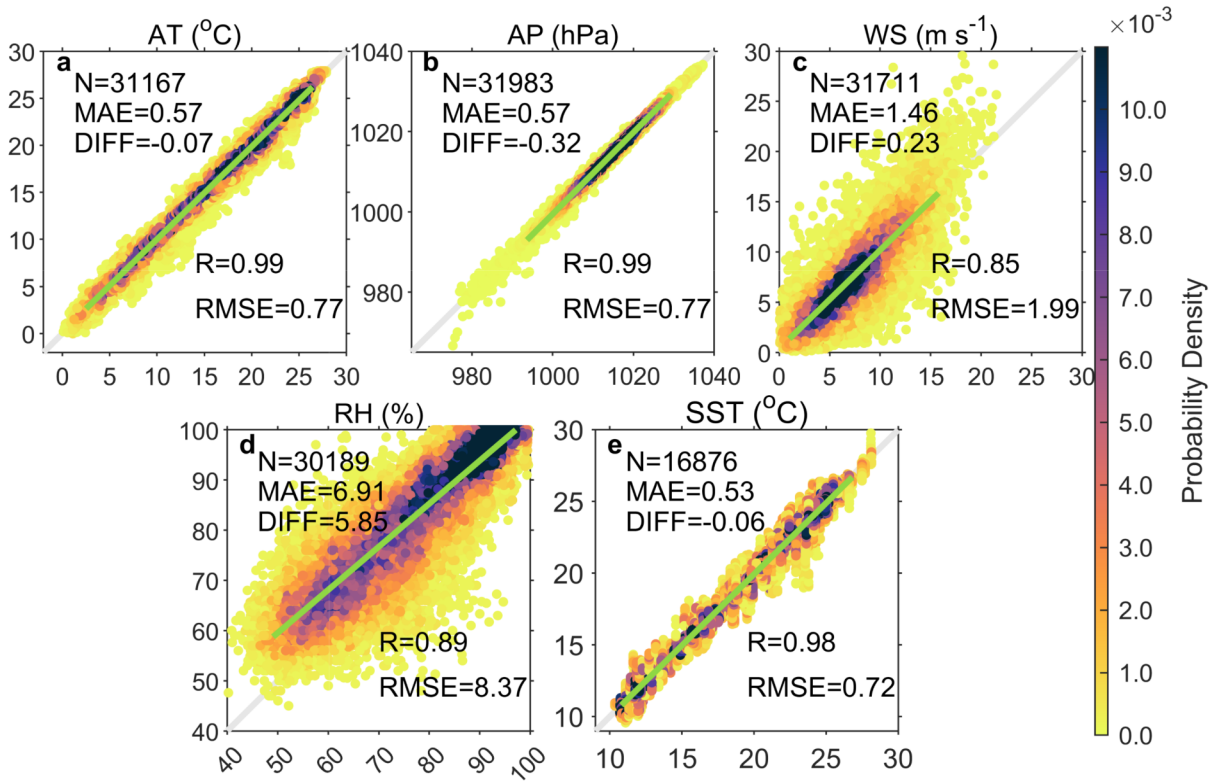

Fig. 8. Density scatterplots of hourly variables collected by the CKEO buoys (*y*-axis) versus ERA5 data (*x*-axis): (a) AT, (b) AP, (c) WS, (d) RH, and (e) SST. The green fitted line corresponds to the linear regression of the data points. The color of the scatter represents the probability density of the occurrence of that value in a given bin. N: data volume of the quality-controlled parameters; MAE: mean absolute error; DIFF: mean difference (CKEO minus ERA5); R: correlation coefficient; RMSE: root-mean-square error.

nounced oceanic and atmospheric responses to the typhoon.

During the passage, WS increased sharply, while AP dropped to a minimum of 984 hPa (Fig. 10b). At the same time, Krosa (2025) also induced a significant decrease in RH. The strong wind field further enhanced the wave intensity, with the significant wave height reaching 10 m (Fig. 10c).

The passage of Krosa (2025) enhanced vertical mixing at the base of the mixed layer and the upper thermocline and induced Ekman suction, leading to a cooling in mixed-layer temperature. Both AT and SST dropped simultaneously, with the SST decline persisting until about 9 August. Prior to Krosa (2025)'s passage, the 20°C isotherm in the upper ocean was generally located within the 20–30 m depth range. Following the typhoon, on 3 and 4 August, the isotherm shoaled upward due to the suction effect, characterized by two distinct episodes in which the SST dropped below 20°C. From 3 to 10 August, the isotherm continued fluctuating under the influence of Krosa (2025) (Figs. 10d, e).

The upper-ocean response to the passage of Krosa (2025) can be divided into two phases (Sanford et al., 1987, 2007, 2011; Shay et al., 1998). The first phase is the "forced stage", during which the typhoon induced strong currents within the mixed layer. The second phase is the "relaxation stage", when the energy input by the typhoon into the mixed layer propagated downward into deeper waters in the form of near-inertial internal waves.

On the right-hand side of a typhoon track in the Northern Hemisphere, the wind field rotates clockwise, making it more prone to resonate with the current field (Price, 1981), thereby exciting near-inertial internal wave signals. Based on the buoy data, the wind-induced near-inertial energy flux shows a pronounced positive peak on 2 August. This peak indicates that during Krosa (2025)'s passage, a substantial amount of near-inertial energy was injected into the ocean, reaching up to approximately 280 mW m^{-2}. In the following days, most of the near-inertial energy was confined to the upper 30 m in the form of near-inertial oscillations. Although Krosa (2025)'s direct influence was relatively short-lived, part of the near-inertial energy could still be observed propagating downward in the form of near-inertial internal waves, extending below the mixed layer and even into deeper layers (Fig. 10h). The near-inertial kinetic energy (NIKE) is calculated as follows:

$$\mathrm{NIKE} = 0.5\rho(u_i^2 + v_i^2)\,, \tag{1}$$

where u_i and v_i are the two components of the near-inertial current velocity, and ρ is the seawater density, which is taken here as 1024 kg m^{-3}. The near-inertial velocity (Figs. 10f, g) is obtained by applying a bandpass filter to the observed current velocity, with the passband selected based

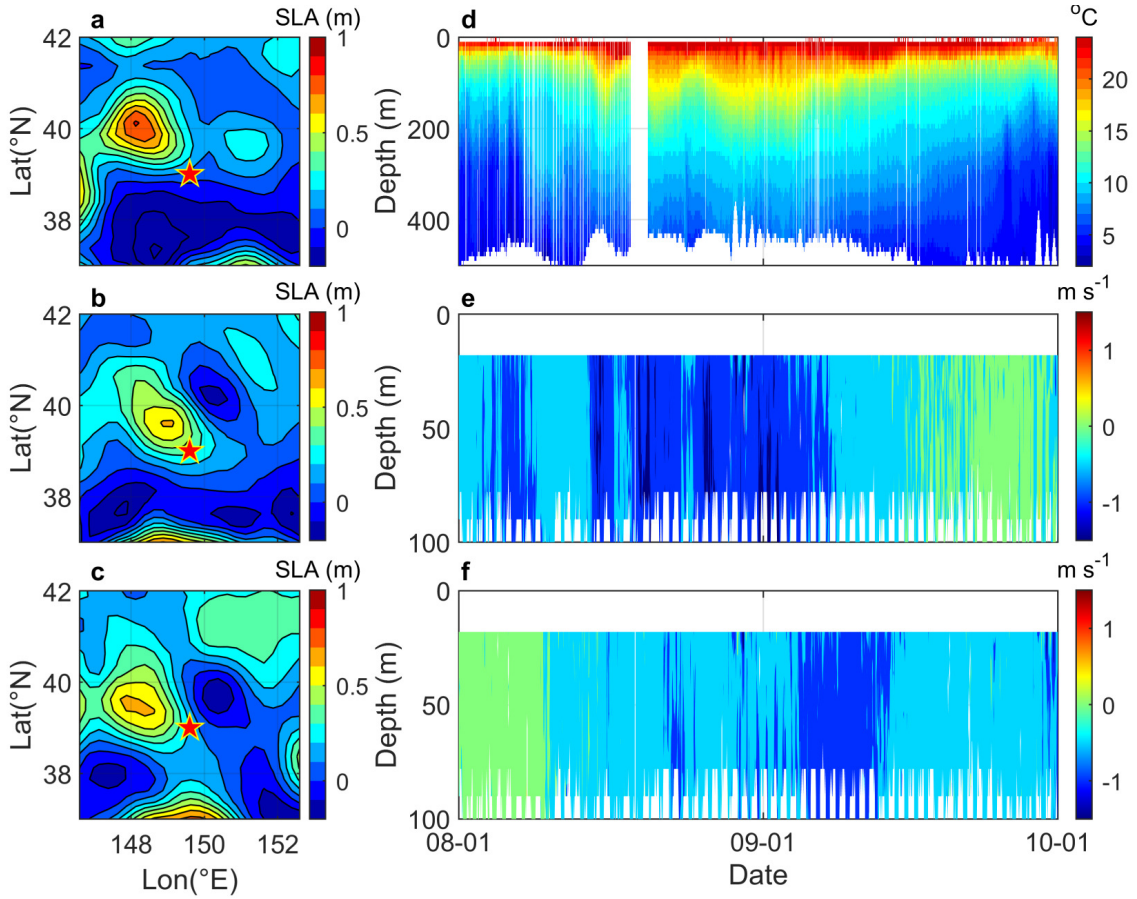

Fig. 9. Satellite-derived SLA on (a) 20 July, (b) 20 August, and (c) 9 September 2023. The moored buoy location is marked by a red star. Time–depth profiles of (d) temperature and (e) zonal and (f) meridional velocity profiles from buoy observations spanning 1 August to 1 October 2023. The SLA data are from the Copernicus Marine Service's "Global Ocean Gridded L4 Sea Surface Heights And Derived Variables Reprocessed" product (https://dx.doi.org/10.48670/moi-00148).

on the deployment latitude of the buoy (39°N).

6. Summary and discussion

6.1. *Summary*

The CKEO for long-term observations in the KOTZ is introduced in terms of its overall design, mooring system, sensor suite, data collection, and QC. The CKEO provides a time series of meteorological and oceanographic properties from 2019 to date, despite encountering data discontinuity owing to various environmental and technical problems. The dataset includes sea surface wind, AT, AP, RH, SST, salinity, ocean current profiles for the upper 100 m, and temperature for the upper 500 m. Data comparisons and two case studies involving an eddy and a typhoon reveal the promising performance of the CKEO. Following the discontinuation of the JKEO program, the CKEO and the KEO are currently the only long-term moored air–sea observatories in the region. Positioned north of the Kuroshio main axis, the CKEO, together with its counterpart, the KEO, to the south of the KE jet, provides valuable complementary data to the scientific community, filling critical gaps for advancing the understanding of air–sea interaction and mesoscale processes in this harsh environment.

6.2. *Reasons for the data discontinuity of the CKEO*

The CKEO has experienced multiple medium- to long-term data gaps attributable to several factors. Diagnosis revealed that two solar panels on CKEO-03 were lost due to harsh sea conditions from May 2021 to June 2022. The insufficient solar panel capacity led to prolonged low battery voltage during winter, ultimately triggering a system shutdown. During the fourth (CKEO-04, 2022–2023) and sixth (CKEO-06, 2024–2025) deployments, the sealing of the central control cabin was compromised, allowing seawater to enter the cabin and causing a short circuit in the power system. This incident led to the shutdown of the control unit and subsequently severed the satellite communication link, resulting in a significant data gap. The CKEO also faced intentional destruction by fishermen. It is believed that the upper structure, including the antennas and meteorological sensors, of CKEO-05 from 2023 to 2024, was dismantled (as shown in Fig. 4). This man-made sabotage led to the failure of the cen-

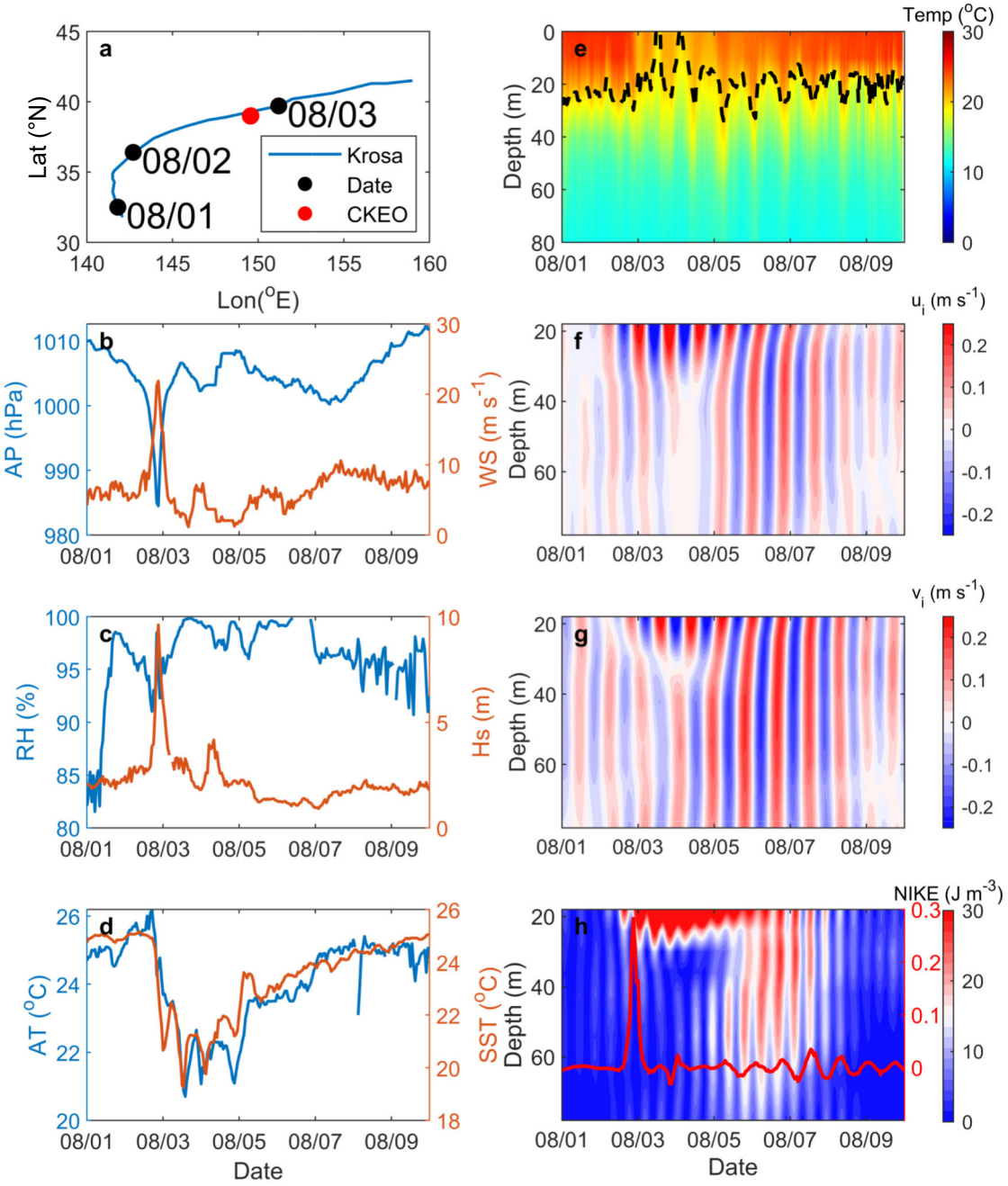

Fig. 10. (a) Track of Typhoon Krosa (2025) and the location of the CKEO buoy. (b) AP and WS. (c) RH and significant wave height (observed by a 9-axis accelerometer of the CKEO; beta version, not publicly available yet). (d) AT and SST. (e) Upper-ocean temperature, with the black dashed line indicating the 20°C isotherm. (f) Upper-ocean near-inertial zonal velocity. (g) Upper-ocean near-inertial meridional velocity. (h) Upper-ocean NIKE, with the red solid line denoting the wind input of near-inertial energy (units: mW m^{-2}).

tral control system and a complete interruption of data acquisition, resulting in over six months of data loss.

6.3. *Technical challenges of the CKEO*

The CKEO began observations in 2019, and after six years of operation, we found that the most pressing technical challenge lies in optimizing the power management system. During winter, solar panels face reduced power generation due to low solar altitude and the accumulation of salt spray, bird droppings, and ice. Additionally, the communication system, a major power consumer, struggles with icing on the antennas, leading to communication failures and increased power consumption.

These challenges result in inadequate recharging of the power system, causing battery levels to drop and the central control system to enter the power protection mode, shutting down sensors and communication modules and creating "data gaps". To address this, the CKEO team plans to opti-

mize the power management system, incorporate a remote watchdog for real-time monitoring of communication logs, and implement strategies for automatic data recovery after power restoration.

Another concern is data interruptions from underwater inductive sensors due to the significant vertical movement of the buoy in severe sea conditions, which can misalign the instruments. Biofouling also reduces communication efficiency. Future upgrades will focus on enhancing the structural stability of the inductive module, applying anti-fouling coatings, and establishing a real-time diagnostic system for underwater coupling status.

6.4. *Perspective*

The integrated CKEO buoy system offers a unique opportunity to explore the formation and evolution mechanisms of North Pacific subtropical mode water and quantify the modulation of its dynamics by submesoscale processes. By combining high-frequency meteorological measurements with upper-layer CTD profiles, the CKEO delineates the mixed layer's seasonal cycle—from winter deepening to spring restratification—and quantifies the surface buoyancy forcing that drives the formation of North Pacific subtropical mode water.

Through the documentation of extreme events, CKEO data will facilitate assessments of the persistence and decay of marine heatwaves, as well as their impacts on boundary layer stability and the development of high-impact weather systems, including heavy precipitation and extratropical cyclones. By delivering high-quality measurements of surface fluxes and state variables in the KOTZ, the CKEO will enhance the refinement of bulk flux algorithms and coupled model parameterizations.

The addition of an ADCP has significantly enhanced our ability to resolve high-frequency variability in the upper ocean. The ADCP also measures the backscatter intensity related to biological concentrations, allowing high-resolution observations of zooplankton abundance and their diel vertical migration behaviors. In the future, a fishing echo sounder will be added to the CKEO, facilitating zooplankton observations.

Beyond advancing scientific understanding, the CKEO will improve the accuracy of other data sources, aiding satellite calibration and validation, as well as the evaluation of numerical weather prediction and reanalysis products. Its strategic location and continuous operation will contribute significantly to our understanding of western boundary current regions, ultimately enriching our insights into climate dynamics and oceanic processes.

Acknowledgements. This research was supported by the Natural Science Foundation of China (Grant No. 42225601), the Laoshan Laboratory (Grant No. LSKJ202201601), the Fundamental Research Funds for the Central Universities (Grant Nos. 202072001 and 202241006), and the Supporting Funds for Leading Talents (Grant No. 2022GJJLJRC02-014). We would like to express our gratitude for the strong support from the captains and all crew members of the RV DFH3 over the past six years.

REFERENCES

Alford, M. H., 2003: Improved global maps and 54-year history of wind-work on ocean inertial motions. *Geophys. Res. Lett.*, **30**, 1424, https://doi.org/10.1029/2002GL016614.

Bond, N. A., M. F. Cronin, C. Sabine, Y. Kawai, H. Ichikawa, P. Freitag, and K. Ronnholm, 2011: Upper ocean response to Typhoon Choi-Wan as measured by the Kuroshio Extension Observatory mooring. *J. Geophys. Res.: Oceans*, **116**, C02031, https://doi.org/10.1029/2010JC006548.

Chelton, D. B., M. G. Schlax, and R. M. Samelson, 2011: Global observations of nonlinear mesoscale eddies. *Progress in Oceanography*, **91**, 167–216, https://doi.org/10.1016/j.pocean.2011.01.002.

Cronin, M. F., C. Meinig, C. L. Sabine, H. Ichikawa, and H. Tomita, 2008: Surface mooring network in the Kuroshio Extension. *IEEE Systems Journal*, **2**(3), 424–430, https://doi.org/10.1109/JSYST.2008.925982.

Cronin, M. F., and Coauthors, 2023a: Developing an observing air–sea interactions strategy (OASIS) for the global ocean. *ICES Journal of Marine Science*, **80**(2), 367–373, https://doi.org/10.1093/icesjms/fsac149.

Cronin, M. F., and Coauthors, 2023b: PMEL ocean climate stations as reference time series and research aggregate devices. *Oceanography*, **36**(2–3), 46–53, https://doi.org/10.5670/oceanog.2023.224.

Czaja, A., C. Frankignoul, S. Minobe, and B. Vannière, 2019: Simulating the midlatitude atmospheric circulation: What might we gain from high-resolution modeling of air–sea interactions?. *Current Climate Change Reports*, **5**, 390–406, https://doi.org/10.1007/s40641-019-00148-5.

Di Lorenzo, E., and Coauthors, 2023: Modes and mechanisms of Pacific decadal-scale variability. *Annual Review of Marine Science*, **15**, 249–275, https://doi.org/10.1146/annurev-marine-040422-084555.

Fairall, C. W., E. F. Bradley, J. E. Hare, A. A. Grachev, and J. B. Edson, 2003: Bulk parameterization of air–sea fluxes: Updates and verification for the COARE algorithm. *J. Climate*, **16**, 571–591, https://doi.org/10.1175/1520-0442(2003)016<0571:BPOASF>2.0.CO;2.

Foussard, A., G. Lapeyre, and R. Plougonven, 2019: Storm track response to oceanic eddies in idealized atmospheric simulations. *J. Climate*, **32**(2), 445–463, https://doi.org/10.1175/JCLI-D-18-0415.1.

Frankignoul, C., N. Sennéchael, Y.-O. Kwon, and M. A. Alexander, 2011: Influence of the meridional shifts of the Kuroshio and the Oyashio extensions on the atmospheric circulation. *J. Climate*, **24**, 762–777, https://doi.org/10.1175/2010JCLI3731.1.

Frenger, I., N. Gruber, R. Knutti, and M. Münnich, 2013: Imprint of Southern Ocean eddies on winds, clouds and rainfall. *Nature Geoscience*, **6**(8), 608–612, https://doi.org/10.1038/ngeo1863.

Gan, B. L., and Coauthors, 2023: North Atlantic subtropical mode water formation controlled by Gulf Stream fronts. *National Science Review*, **10**, nwad133, https://doi.org/10.1093/nsr/nwad133.

Hersbach, H., and Coauthors, 2025: ERA5 hourly data on single levels from 1940 to present. Copernicus Climate Change Service (C3S) Climate Data Store (CDS), https://doi.org/10.24381/cds.adbb2d47.

Itoh, S., and I. Yasuda, 2010: Water Mass structure of warm and cold anticyclonic eddies in the western boundary region of the subarctic North Pacific. *J. Phys. Oceanogr.*, **40**, 2624–2642, https://doi.org/10.1175/2010JPO4475.1.

Iwao, T., M. Endoh, N. Shikama, and T. Nakano, 2003: Intermediate circulation in the northwestern North Pacific derived from subsurface floats. *Journal of Oceanography*, **59**, 893–904, https://doi.org/10.1023/B:JOCE.0000009579.86413.eb.

Jing, Z., and L. X. Wu, 2014: Intensified diapycnal mixing in the midlatitude western boundary currents. *Scientific Reports*, **4**, 7412, https://doi.org/10.1038/srep07412.

Jing, Z., and Coauthors, 2020: Maintenance of mid-latitude oceanic fronts by mesoscale eddies. *Science Advances*, **6**(31), eaba7880, https://doi.org/10.1126/sciadv.aba7880.

Jutras, M., S. M. Bushinsky, I. Cerovečki, and N. Briggs, 2025: Mixing accounts for more than half of biogeochemical changes along mode water ventilation pathways. *Geophys. Res. Lett.*, **52**, e2024GL113789, https://doi.org/10.1029/2024GL113789.

Kwon, Y. O., M. A. Alexander, N. A. Bond, C. Frankignoul, H. Nakamura, B. Qiu, and L. A. Thompson, 2010: Role of the gulf stream and Kuroshio–Oyashio systems in large-scale atmosphere–ocean interaction: A review. *J. Climate*, **23**, 3249–3281, https://doi.org/10.1175/2010JCLI3343.1.

Li, X. Y., B. L. Gan, Z. G. Zhang, Z. M. Cao, B. Qiu, Z. H. Chen, and L. X. Wu, 2025: Oceanic uptake of CO_2 enhanced by mesoscale eddies. *Science Advances*, **11**(24), eadt4195, https://doi.org/10.1126/sciadv.adt4195.

Liu, J., L. X. Xu, X.-T. Zheng, K. Y. Wang, and J. L. Li, 2025: Extreme ventilation of the North Pacific Central Mode Water by El Niño during positive phase of the Pacific Decadal Oscillation. *Geophys. Res. Lett.*, **52**, e2024GL113064, https://doi.org/10.1029/2024GL113064.

Liu, X., and Coauthors, 2021: Ocean fronts and eddies force atmospheric rivers and heavy precipitation in western North America. *Nature Communications*, **12**, 1268, https://doi.org/10.1038/s41467-021-21504-w.

Liu, Y. Z., Z. Jing, and L. X. Wu, 2019: Wind power on oceanic near-inertial oscillations in the global ocean estimated from surface drifters. *Geophys. Res. Lett.*, **46**, 2647–2653, https://doi.org/10.1029/2018GL081712.

Ma, X. H., and Coauthors, 2016: Western boundary currents regulated by interaction between ocean eddies and the atmosphere. *Nature*, **535**, 533–537, https://doi.org/10.1038/nature18640.

Ma, X. H., and Coauthors, 2017: Importance of resolving Kuroshio front and eddy influence in simulating the North Pacific storm track. *J. Climate*, **30**(5), 1861–1880, https://doi.org/10.1175/JCLI-D-16-0154.1.

Ma, X. H., and Coauthors, 2024: Midlatitude mesoscale thermal air–sea interaction enhanced by greenhouse warming. *Nature Communications*, **15**, 7699, https://doi.org/10.1038/s41467-024-52077-z.

McPhaden, M. J., K. J. Connell, G. R. Foltz, R. C. Perez, and K. Grissom, 2023: Tropical ocean observations for weather and climate: A decadal overview of the Global Tropical Moored Buoy Array. *Oceanography*, **36**(2–3), 32–43, https://doi.org/10.5670/oceanog.2023.211.

Nagai, T., A. Tandon, E. Kunze, and A. Mahadevan, 2015: Spontaneous generation of near-inertial waves by the Kuroshio Front. *J. Phys. Oceanogr.*, **45**, 2381–2406, https://doi.org/10.1175/JPO-D-14-0086.1.

Polovina, J., I. Uchida, G. Balazs, E. A. Howell, D. Parker, and P. Dutton, 2006: The Kuroshio Extension Bifurcation Region: A pelagic hotspot for juvenile loggerhead sea turtles. *Deep Sea Research Part II: Topical Studies in Oceanography*, **53**(3–4), 326–339, https://doi.org/10.1016/j.dsr2.2006.01.006.

Price, J. F., 1981: Upper ocean response to a hurricane. *J. Phys. Oceanogr.*, **11**, 153–175, https://doi.org/10.1175/1520-0485(1981)011<0153:UORTAH>2.0.CO;2.

Qiu, B., and S. M. Chen, 2005: Variability of the Kuroshio extension jet, recirculation gyre, and mesoscale eddies on decadal time scales. *J. Phys. Oceanogr.*, **35**, 2090–2103, https://doi.org/10.1175/JPO2807.1.

Renault, L., S. Masson, V. Oerder, S. Jullien, and F. Colas, 2019: Disentangling the mesoscale ocean-atmosphere interactions. *J. Geophys. Res.: Oceans*, **124**(3), 2164–2178, https://doi.org/10.1029/2018JC014628.

Sanford, T. B., J. F. Price, and J. B. Girton, 2011: Upper-ocean response to hurricane Frances (2004) observed by profiling EM-APEX floats. *J. Phys. Oceanogr.*, **41**, 1041–1056, https://doi.org/10.1175/2010JPO4313.1.

Sanford, T. B., J. F. Price, J. B. Girton, and D. C. Webb, 2007: Highly resolved observations and simulations of the ocean response to a hurricane. *Geophys. Res. Lett.*, **34**, L13604, https://doi.org/10.1029/2007GL029679.

Sanford, T. B., P. G. Black, J. R. Haustein, J. W. Feeney, G. Z. Forristall, and J. F. Price, 1987: Ocean response to a hurricane. Part 1: Observations. *J. Phys. Oceanogr.*, **17**, 2065–2083, https://doi.org/10.1175/1520-0485(1987)017<2065:ORTAHP>2.0.CO;2.

Sasaki, Y. N., and S. Minobe, 2015: Climatological mean features and interannual to decadal variability of ring formations in the Kuroshio Extension region. *Journal of Oceanography*, **71**, 499–509, https://doi.org/10.1007/s10872-014-0270-4.

Seo, H., and Coauthors, 2023: Ocean mesoscale and frontal-scale ocean–atmosphere interactions and influence on large-scale climate: A review. *J. Climate*, **36**(7), 1981–2013, https://doi.org/10.1175/JCLI-D-21-0982.1.

Shay, L. K., A. J. Mariano, S. D. Jacob, and E. H. Ryan, 1998: Mean and near-inertial ocean current response to hurricane Gilbert. *J. Phys. Oceanogr.*, **28**, 858–889, https://doi.org/10.1175/1520-0485(1998)028<0858:MANIOC>2.0.CO;2.

Small, R. J., and Coauthors, 2008: Air–sea interaction over ocean fronts and eddies. *Dyn. Atmos. Oceans*, **45**(3–4), 274–319,

https://doi.org/10.1016/j.dynatmoce.2008.01.001.

Su, Z., J. B. Wang, P. Klein, A. F. Thompson, and D. Menemenlis, 2018: Ocean submesoscales as a key component of the global heat budget. *Nature Communications*, **9**, 775, https://doi.org/10.1038/s41467-018-02983-w.

Sugimoto, S., 2025: Marine heatwave off Tokai, Japan, attributed to the Kuroshio Large Meander Path, and an associated increase in summer rainfall over Japan. *Journal of Oceanography*, **81**, 63–79, https://doi.org/10.1007/s10872-024-00741-9.

Tomita, H., M. F. Cronin, and S. Ohishi, 2021: Asymmetric air–sea heat flux response and ocean impact to synoptic-scale atmospheric disturbances observed at JKEO and KEO buoys. *Scientific Reports*, **11**, 469, https://doi.org/10.1038/s41598-020-80665-8.

Tsopouridis, L., C. Spensberger, and T. Spengler, 2021: Cyclone intensification in the Kuroshio region and its relation to the sea surface temperature front and upper-level forcing. *Quart. J. Roy. Meteor. Soc.*, **147**, 485–500, https://doi.org/10.1002/qj.3929.

Whalen, C. B., C. De Lavergne, A. C. Naveira Garabato, J. M. Klymak, J. A. MacKinnon, and K. L. Sheen, 2020: Internal wave-driven mixing: Governing processes and consequences for climate. *Nature Reviews Earth & Environment*, **1**, 606–621, https://doi.org/10.1038/s43017-020-0097-z.

Yamamoto, A., and Coauthors, 2018: Roles of the ocean mesoscale in the horizontal supply of mass, heat, carbon, and nutrients to the Northern Hemisphere subtropical gyres. *J. Geophys. Res.: Oceans*, **123**, 7016–7036, https://doi.org/10.1029/2018JC013969.

Yang, H. Y., B. Qiu, P. Chang, L. X. Wu, S. P. Wang, Z. H. Chen, and Y. Yang, 2018: Decadal variability of eddy characteristics and energetics in the Kuroshio Extension: Unstable versus stable states. *J. Geophys. Res.: Oceans*, **123**, 6653–6669, https://doi.org/10.1029/2018JC014081.

Yasuda, I., 2003: Hydrographic structure and variability in the Kuroshio–Oyashio transition area. *Journal of Oceanography*, **59**, 389–402, https://doi.org/10.1023/A:1025580313836.

Yatsu, A., S. Chiba, Y. Yamanaka, S. I. Ito, Y. Shimizu, M. Kaeriyama, and Y. Watanabe, 2013: Climate forcing and the Kuroshio/Oyashio ecosystem. *ICES Journal of Marine Science*, **70**(5), 922–933, https://doi.org/10.1093/icesjms/fst084.